

---

# CHAPTER

---

# 3

## Beaches morphodynamic modeling based on Hadamard Sensitivity Analysis

---

*In the last chapter, we have selected some interesting wave models for incorporation into our OptiMorph model. However, the OptiMorph model in its chapter 1 version couldn't couple just any wave model, as there was the need to calculate a particular gradient (with respect to shape), which was done analytically. In this chapter, we presents a morphodynamic model which can be coupled with any wave model capable of producing time/spectral averaged wave quantities. This model based on a wave energy minimization principle highlights the morphodynamic phenomenology, such as the sandbar creation. Such a model can be used in solving engineering optimization problems. It is also developed to illustrate the idea that beach sand transport can be thought as a non-local phenomenon. We used wave calculations from SWAN, XBeach and Shallow-Water in our model, and we compared the morphodynamic results to LIP and SANDS hydro-morphodynamic benchmark as well as open-sea simulations. Using supplementary mathematical development, we improved the minimization method using the Hadamard derivative.*

---

---

### Current chapter contents

---

<b>1</b>	<b>Introduction . . . . .</b>	<b>98</b>
<b>2</b>	<b>Gradient Calculation with Respect to the Shape <math>\nabla_{\psi}\mathcal{J}</math> . . . . .</b>	<b>99</b>
2.1	Analytical Calculation of $\nabla_{\psi}H$ . . . . .	99
2.2	Finite Difference Calculation of $\nabla_{\psi}H$ . . . . .	100
2.3	Automatic Differentiation (AD) Method to Calculate $\nabla_{\psi}H$ . . . . .	101
2.3.1	Direct and Reverse modes of Automatic Differentiation . . . . .	101
<b>3</b>	<b>Using Hadamard for the Calculation of <math>\nabla_{\psi}\mathcal{J}</math> . . . . .</b>	<b>101</b>
3.1	Principle . . . . .	101
3.2	Analytical Examples of Hadamard Derivative . . . . .	102
3.2.1	Flat form . . . . .	102
3.2.2	Linear Form . . . . .	103
3.3	Numerical Validation . . . . .	105
3.4	Validating the Hadamard Solution . . . . .	106
<b>4</b>	<b>Application of Hadamard Strategy . . . . .</b>	<b>107</b>

4.1	Description of Flumes Experiments . . . . .	108
4.1.1	The SANDS Experiments . . . . .	108
4.1.2	The LIP Experiments . . . . .	109
4.2	Hydro-Morphodynamic Results on Flume Experiment . . . . .	110
4.3	Hydro-Morphodynamic Results on Open-sea Configurations . . . . .	112
5	<b>Discussion</b> . . . . .	114
5.1	Computation time . . . . .	114
5.2	Flume Simulation . . . . .	115
5.3	Open-Sea Simulation . . . . .	117
5.4	Gamma Sensibility . . . . .	118
5.5	Limitation of a Wave Resolving Model . . . . .	118
6	<b>Conclusion</b> . . . . .	119

---

## 1 Introduction

MORPHODYNAMIC MODELS are generally very complex and highly parameterized. They separately solve the physical equations of hydrodynamics and morphodynamics at a very small scale of the order of second in time and of the wave length in space. The OptiMorph model that we presented in [Cook \(2021\)](#) and [Ronan Dupont et al. \(2023\)](#) proposes a more global approach based on an optimization principle.

The optimization theory is the study of the evolution of a system while searching systematically for the minimum of a function derived from some of its physical properties. Using a certain number of mathematical optimization developments devoted to coastal sciences ([Isèbe et al. 2014](#); [Isèbe et al. 2008b](#); [Isèbe et al. 2008a](#); [Bouharguane et al. 2010](#); [Mohammadi et al. 2014](#); [Mohammadi et al. 2011](#); [Cook et al. 2021c](#); [Mohammadi 2017](#); [Bouharguane et al. 2012](#); [Ronan Dupont et al. 2022](#); [Ronan Dupont et al. 2023](#)), we have designed a model that describes the evolution of the sea bottom elevation while taking into account the coupling between morphodynamic and wave processes. This study is based on the assumption that the sea bottom adapts in time to minimize a certain wave-related function. The choice of this function determines the driving force behind the morphological evolution of the seabed. This optimization problem is subjected to a limited number of constraints, allowing for a more accurate description of the morphodynamic evolution.

The purpose of this study is to use the [Hadamard \(1914\)](#) derivative in order to calculate the gradient of any cost function  $\mathcal{J}$  with respect to the shape  $\psi$ , which allows us to solve the optimization problem at the core of the model. This strategy aims to create a generic morphodynamic model that can be used with any wave model.

The chapter starts with the Hadamard's strategy by presenting the different ways to compute the gradient with respect to the shape  $\psi$ . Hadamard's strategy is verified

with analytical cases. Finally, applications are performed with OptiMorph model using Hadamard strategy. We show that we can therefore use complex wave models such as XBeach (D. J. Roelvink et al. 2009), SWAN (Booij et al. 1996) and Shallow-Water (Marche et al. 2007). Part of the simulations are linked to the LIP and SANDS flume experiments (Roelvink et al. 1995; Eichentopf et al. 2018). Another part concerns simulations in open-sea configurations.

## 2 Gradient Calculation with Respect to the Shape $\nabla_\psi \mathcal{J}$

Calculation of  $\nabla_\psi \mathcal{J}$  is necessary to do shape optimization with descent method equation (5.16). This quantity is not easy to compute since we do not differentiate on an axis but on a shape  $\psi$ .  $\mathcal{J}$  depends on wave height  $H$ ; it is thus advisable to have a very simple wave model in order to differentiate it easily. We assume at first that  $\mathcal{J}$  is of the form  $\mathcal{J}(H(\psi(x)))$  involving dependencies with respect to wave quantities  $H$ . This sensitivity is given by:

$$\begin{aligned} \nabla_\psi \mathcal{J} &= \nabla_H \mathcal{J} \nabla_\psi H, \\ &= \nabla_H \left( \frac{1}{16} \rho g H^2 \right) \nabla_\psi H, \\ &= \frac{1}{8} \rho g H \nabla_\psi H. \end{aligned} \tag{3.1}$$

Calculating  $\nabla_\psi \mathcal{J}$  reduces to that of  $\nabla_\psi H$ . It can be done analytically using the simple shoaling model described in equations (1.2a) and (1.2b) as described later in section 2.1. One can also use a heavy formalism like automatic differentiation (Hascoet et al. 2004; Mohammadi et al. 2011). These strategies are described below and in section 3, where we show how to obtain  $\nabla_\psi H$  whatever may be our functions  $H$  and  $\psi$ .

### 2.1 Analytical Calculation of $\nabla_\psi H$

The analytical method is the most precise (because it gives the exact value) and the fastest in calculation time. To illustrate the purpose, we take equation (1.2a) of  $H$  and we differentiate them in the following way:

$$\nabla_\psi H = \begin{cases} H_0(t) \nabla_\psi Ks(x, h) & \text{pour } x \in \Omega_S \\ \gamma \nabla_\psi h(x, t) & \text{pour } x \in \Omega_B \end{cases}. \tag{3.2}$$

The problem is reduced to the calculation of  $\nabla_{\psi} K_S(x, t)$  and  $\nabla_{\psi} h(x, t)$ . The relation  $h = h_0 - \psi$  ensures that  $\nabla_{\psi} h(x, t) = -1$ . Moreover, we have:

$$K_S = \left[ \tanh(kh) \left( 1 + \frac{2kh}{\sinh(2kh)} \right) \right]^{-1/2}. \quad (3.3)$$

Let  $U(X) = \tanh(X) \left( 1 + \frac{2X}{\sinh(2X)} \right)$  and  $X = kh$ . Introducing  $U$  in equation (3.3) and derivating  $\psi$  results in:

$$\nabla_{\psi} K_S = -\frac{1}{2} U^{-3/2} \nabla_{\psi} U. \quad (3.4)$$

By trigonometric transformation, we can demonstrate that:

$$\nabla_{\psi} U = \nabla_{\psi} X \frac{2 \cosh^2(X) - X \sinh(2X)}{\cosh^4(X)}, \quad (3.5)$$

we also have:

$$\nabla_{\psi} X = h \nabla_{\psi} k + k \nabla_{\psi} h = h \nabla_{\psi} k - k. \quad (3.6)$$

Moreover, differentiating both sides of the dispersion equation  $\sigma^2 = gk \tanh(kh)$  by  $\psi$  gives

$$\nabla_{\psi} k = \frac{k^2}{\cosh(kh) \sinh(kh) + kh}. \quad (3.7)$$

Combining (3.4), (3.5), and (3.7), we obtain  $\nabla_{\psi} K_S$ , and therefore  $\nabla_{\psi} H$ , on  $\Omega_S$ .

This method is the most accurate and robust because it gives the analytical solution directly. However, it is applicable to a very limited number of wave models. Indeed, they must be very simple to be differentiated by hand. Our ambition is to have a strategy that may allow to differentiate the mathematical representation of any hydrodynamic.

## 2.2 Finite Difference Calculation of $\nabla_{\psi} H$

Finite difference methods are based on the idea of approximating the derivative of a function at a point by taking the difference between the values of the function at two adjacent points. Considering the directional gradient formula at  $\psi$  along direction  $l$ :

$$\nabla_{\psi} H(\psi) = \lim_{\varepsilon \rightarrow 0} \frac{H(\psi + \varepsilon l) - H(\psi)}{\varepsilon}. \quad (3.8)$$

We could define a first order finite difference approximation of the gradient at  $\psi \in \mathbb{R}^N$

taking for  $l$  the vectors  $e_{i=1,\dots,N}$  of the canonical basis of  $\mathbb{R}^N$ . The  $i^{th}$  evaluation provides the corresponding component of the gradient vector. This method requires  $N + 1$  evaluation of the wave model which makes the method computationally expensive, as it can be classically of the order of several thousand runs in practice.

## 2.3 Automatic Differentiation (AD) Method to Calculate $\nabla_\psi H$

Automatic differentiation (AD) of programs is an important tool for numerical optimization and scientific computing. It is a technique for computing derivatives of a given program by successive derivation of the lines of the code. AD can be used to compute derivatives of functions with respect to both scalar and vector variables (Griewank et al. 2008).

### 2.3.1 Direct and Reverse modes of Automatic Differentiation

Direct AD uses the chain rule to compute derivatives of a program with respect to the input parameters of the code. The direct AD method can be used to compute derivatives of functions of any order, including higher-order derivatives. This method is relatively simple to implement, and is often used when the number of input variables is small. On the other hand, when the size of input variables is large, the reverse mode of AD is used. The computation cost is independent of the size of the inputs. A typical AD tool is the TAPENADE program (Hascoet et al. 2004) which provides Fortran or C codes for the derivatives of programs in direct and reverse modes. This means that we need to provide the source code. As a consequence, the main limitation of this approach is that it cannot be applied to a commercial code when the source code is not provided. Even when the code is provided (open source), it is written in a modular way, which makes it very difficult to isolate the variables to differentiate.

## 3 Using Hadamard for the Calculation of $\nabla_\psi \mathcal{J}$

In this section, we focus on the calculation of  $\nabla_\psi H$  in order to obtain  $\nabla_\psi \mathcal{J}$  (as illustrated in section 2). This method can be applied whatever may be the variables: we can directly calculate  $\nabla_\psi \mathcal{J}$ . However, in this case, the approximation would be less good because the analytical derivative of  $\mathcal{J}$  (equation (3.1)) is always more accurate.

### 3.1 Principle

We use the approximation described in (Hadamard 1914; Mohammadi 2007; Mohammadi 2010). We consider  $\nabla_\psi H$  in the sense of Hadamard following the definition:

$$\nabla_{\psi} H = \lim_{\varepsilon \rightarrow 0} \frac{H(\psi + \varepsilon n) - H(\psi)}{\varepsilon}, \quad (3.9)$$

where  $n$  is the normal to the shape  $\psi$ . This can be seen as applying a [Gâteaux \(1913\)](#) derivation in the direction normal to the shape. The principle is illustrated in figure 5.7.

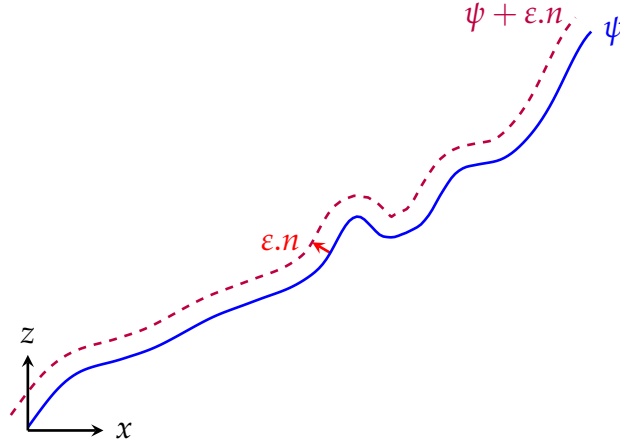


**Figure 3.1** – Representation of two sea bottom profiles  $\psi$  and  $\psi + \varepsilon n$ . To calculate the gradient, we need to calculate at all points the associated normal vector  $n$ .

Using the Taylor-Young formula at order 1, we consider the following approximation:

$$\begin{aligned} \nabla_{\psi} H &= \lim_{\varepsilon \rightarrow 0} \frac{H(\psi) + \varepsilon \nabla_X H \cdot n - H(\psi)}{\varepsilon}, \\ &\approx (\nabla_X H) \cdot n, \end{aligned} \quad (3.10)$$

with  $X = (x, z)^T$ . This approximation is illustrated in the following section 3.2 on simple analytical examples; and also on the simple shoaling model in section 3.4.

## 3.2 Analytical Examples of Hadamard Derivative

In this section, we illustrate analytical examples of derivation of  $\psi$  on a quantity  $A$ ; concretely, we calculate  $\nabla_{\psi} A$ .

### 3.2.1 Flat form

We consider the relation  $A = \psi^2$ . We set in a general way  $\psi = \{(x, y) \in \mathbb{R}^2 \mid y - f_{\psi}(x) = 0\}$  the space of  $\psi$  with  $f_{\psi}$  the function describing the bottom. The flat form  $\psi = \{(x, y) \in \mathbb{R}^2 \mid y - c = 0\}$  deformed from  $\varepsilon n$  is given by  $\psi + \varepsilon n = \{(x, y) \in \mathbb{R}^2 \mid y - c - \varepsilon = 0\}$ . It could be illustrated by the figure 3.1.

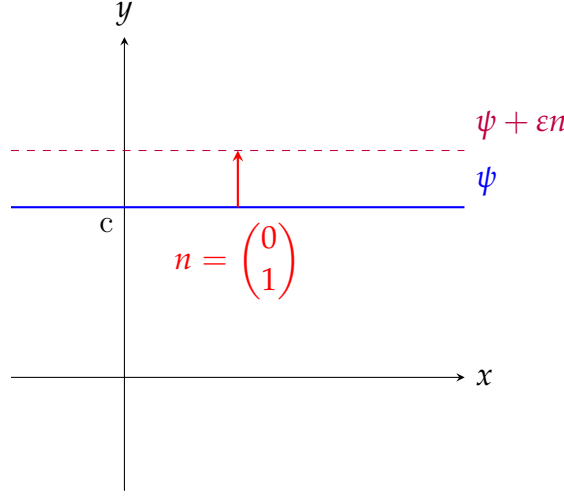


**Figure 3.1** – Illustration of  $\psi$  and  $\psi + \epsilon n$  with the function  $\psi : x \rightarrow c$

Here we have:

$$\psi = \{(x, y) \in \mathbb{R}^2 \mid y - c = 0\} \text{ and } A = \psi^2 = \{(x, y) \in \mathbb{R}^2 \mid y - c^2 = 0\},$$

then, we have, thank to the definition, on the one hand:

$$\begin{aligned} \nabla_\psi A &= \lim_{\epsilon \rightarrow 0} \left( \frac{1}{\epsilon} [A(\psi + \epsilon n) - A(\psi)] \right), \\ &= \lim_{\epsilon \rightarrow 0} \left( \frac{1}{\epsilon} [\cancel{\psi^2} + 2\psi\epsilon + \underbrace{\epsilon^2}_{\rightarrow 0} - \cancel{\psi^2}] \right) \quad \text{because } A(\psi + \epsilon n) = (\psi + \epsilon)^2, \\ &= 2\psi, \end{aligned}$$

on the other hand:

$$\nabla_X A.n = 2\psi \nabla_X(\psi).n = 2\psi \begin{pmatrix} 0 \\ 1 \end{pmatrix} \begin{pmatrix} 0 \\ 1 \end{pmatrix} = 2\psi, \quad (3.1)$$

and therefore

$$\nabla_X A.n = \nabla_\psi A. \quad (3.2)$$

### 3.2.2 Linear Form

The linear form  $\psi = \{(x, y) \in \mathbb{R}^2 \mid y - ax - b = 0\}$  deformed by  $\epsilon n$  is given by  $\psi + \epsilon n$ . We consider the relation  $A = \cos(\psi)$ . We set in a general way  $\psi = \{(x, y) \in \mathbb{R}^2 \mid y - f_\psi(x) = 0\}$  the space of  $\psi$  with  $f_\psi$  the function describing the bottom. It could be illustrated by

the figure 3.2.

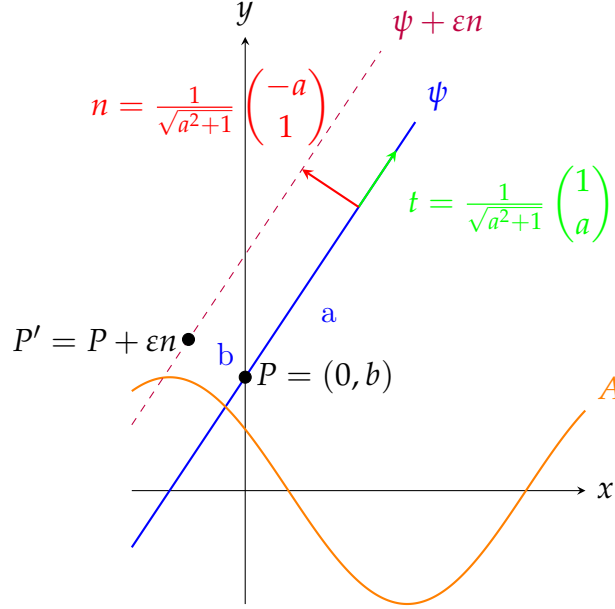


**Figure 3.2** – Illustration of  $\psi$ ,  $\psi + \varepsilon n$  and  $A$  with the function  $\psi : x \rightarrow ax + b$  and  $A = \cos(\psi)$

We know the point  $P(0, b)$  is contained on the line. The point  $P' = P + \varepsilon n$  is therefore contained on the new translated line. We deduce the equation rapidly:

$$\psi + \varepsilon n = ax + \varepsilon \sqrt{a^2 + 1} + b. \quad (3.3)$$

Let us check the equation (5.21) for  $A = \cos(\psi)$ . On the one hand, we have:

$$\begin{aligned} \nabla_{\psi} A &= \lim_{\varepsilon \rightarrow 0} \left( \frac{1}{\varepsilon} [A(\psi + \varepsilon n) - A(\psi)] \right), \\ &= \lim_{\varepsilon \rightarrow 0} \left( \frac{1}{\varepsilon} [\cos(ax + \varepsilon \sqrt{a^2 + 1} + b) - \cos(ax + b)] \right), \\ &= \lim_{\varepsilon \rightarrow 0} \left( \frac{1}{\varepsilon} [\cos(ax + b) \underbrace{[\cos(\varepsilon \sqrt{a^2 + 1}) - 1]}_{\rightarrow -1 - \varepsilon^2(a^2 + 1)} - \sin(ax + b) \underbrace{\sin(\varepsilon \sqrt{a^2 + 1})}_{\rightarrow \varepsilon \sqrt{a^2 + 1}}] \right), \\ &= \lim_{\varepsilon \rightarrow 0} \left( \underbrace{-\cos(ax + b) \varepsilon (a^2 + 1)}_{\rightarrow 0} - \sin(ax + b) \sqrt{a^2 + 1} \right), \\ &= -\sin(\psi) \sqrt{a^2 + 1}. \end{aligned}$$



On the other hand, we have:

$$\nabla_X A = -\sin(\psi) \nabla_X \psi = -\sin(\psi) \begin{pmatrix} -a \\ 1 \end{pmatrix}, \quad (3.4)$$

and therefore:

$$\nabla_X A.n = -\frac{\sin(\psi)}{\sqrt{a^2+1}} \begin{pmatrix} -a \\ 1 \end{pmatrix} \begin{pmatrix} -a \\ 1 \end{pmatrix} = -\sin(\psi) \frac{(a^2+1)}{\sqrt{a^2+1}} = -\sin(\psi) \sqrt{a^2+1}. \quad (3.5)$$

The equality:  $\nabla_\psi A = \nabla_X A.n$  is still verified.

### 3.3 Numerical Validation

The approximation (5.21) can be verified by calculating numerically the solution of the analytical example presented in the section 3.2.2. We calculate the error  $L^2$  named  $\mathcal{E}_{L^2} = \|(\nabla_\psi H)_{\text{exact}} - (\nabla_\psi H)_{\text{numerical}}\|_{L^2}$  for points which correspond to the spatial steps  $dx = [10^{-5}, 10^{-4}, 10^{-3}, 10^{-2}, 0.1, 1, 10, 100]$  for a length  $L = 1000$  m. We obtain the curves in figure 3.3.

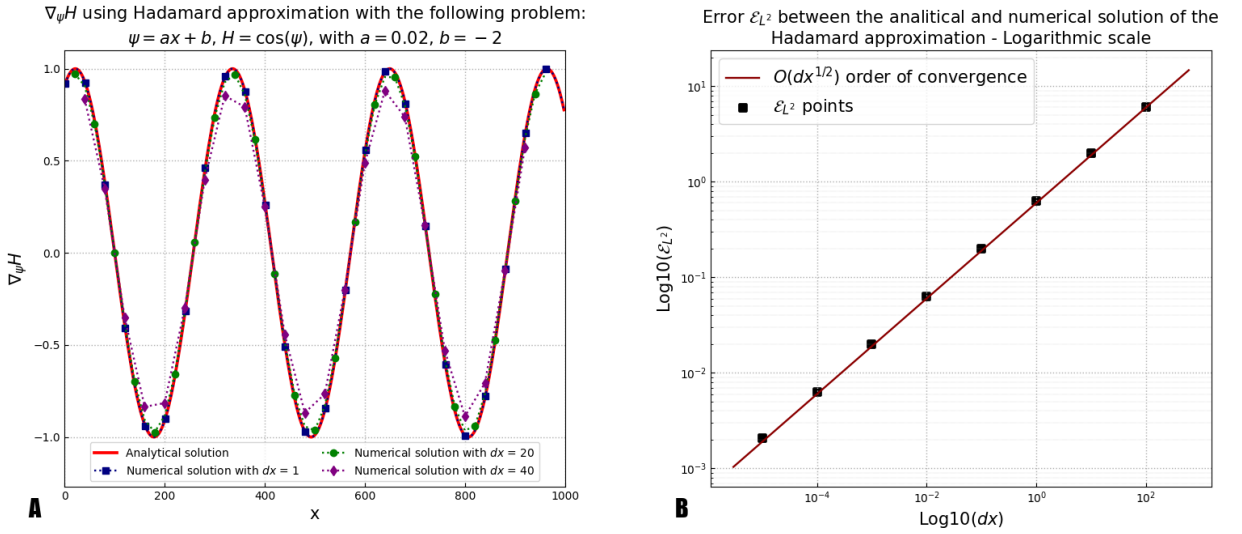


**Figure 3.3** – A) Calculation of  $\nabla_\psi H$  using Hadamard approximation with the following problem (see 3.2.2):  $\psi = ax + b$ ,  $H = \cos(\psi)$ , with  $a = 0.02$ ,  $b = -2$ . B)  $L^2$  error and order of convergence for a comparison between the analytical solution of the simple problem described in 3.2.2 with  $H = \cos(\psi)$ .

We notice that the approximation becomes good very quickly. On the figure 3.3.A, we see that an increment  $dx = 20$  m is enough to reach an almost perfect approximation. The figure 3.3.B shows that the error is very small and converges to the order  $\mathcal{O}(dx^{1/2})$ . The sources of error for this calculation could be a) the approximation in the calculation of the vector  $n$  (in this case, it is null because  $\psi$  is linear), b) the computation of the

gradient by finite differences (order 1).

### 3.4 Validating the Hadamard Solution

Historically, the OptiMorph model used the shoaling equation equations (1.2a) and (1.2b) and was based on the analytical differentiation of this equation (section 2.1). The Hadamard strategy allows us to obtain a calculation of  $\nabla_{\psi}H$  in a numerical way, as with finite differences. To implement this approach practically, we simply need to use the equation (5.21) with:  $\nabla_X H = \begin{pmatrix} \frac{\partial H}{\partial x} \\ \frac{\partial H}{\partial \psi} \end{pmatrix}$  and  $n = \frac{1}{\sqrt{d\psi^2 + dx^2}} \begin{pmatrix} -d\psi \\ dx \end{pmatrix}$  and we obtain:

$$\nabla_{\psi}H \approx \frac{\partial H}{\partial x}n_x + \frac{\partial H}{\partial \psi}n_z, \quad (3.6)$$

with  $n_x$  and  $n_z$  the  $x$  and  $z$  component of  $n$ . In OptiMorph, we implement equation (5.22) and we compare the calculations of  $\nabla_{\psi}H$  using the simple shoaling model presented in equations (1.2a) and (1.2b). The figure 3.4 shows a comparison of the Hadamard and exact solutions on a representative example: an offshore water level  $H_0 = 2$  m, an offshore water depth  $h_0 = 10$  m, a wave period  $T_0 = 10$  s and a linear bottom profile  $\psi$ . The figure 3.4.A corresponds to a simple case and the figure 3.4.B to a case with small scales perturbations of the sea bottom.

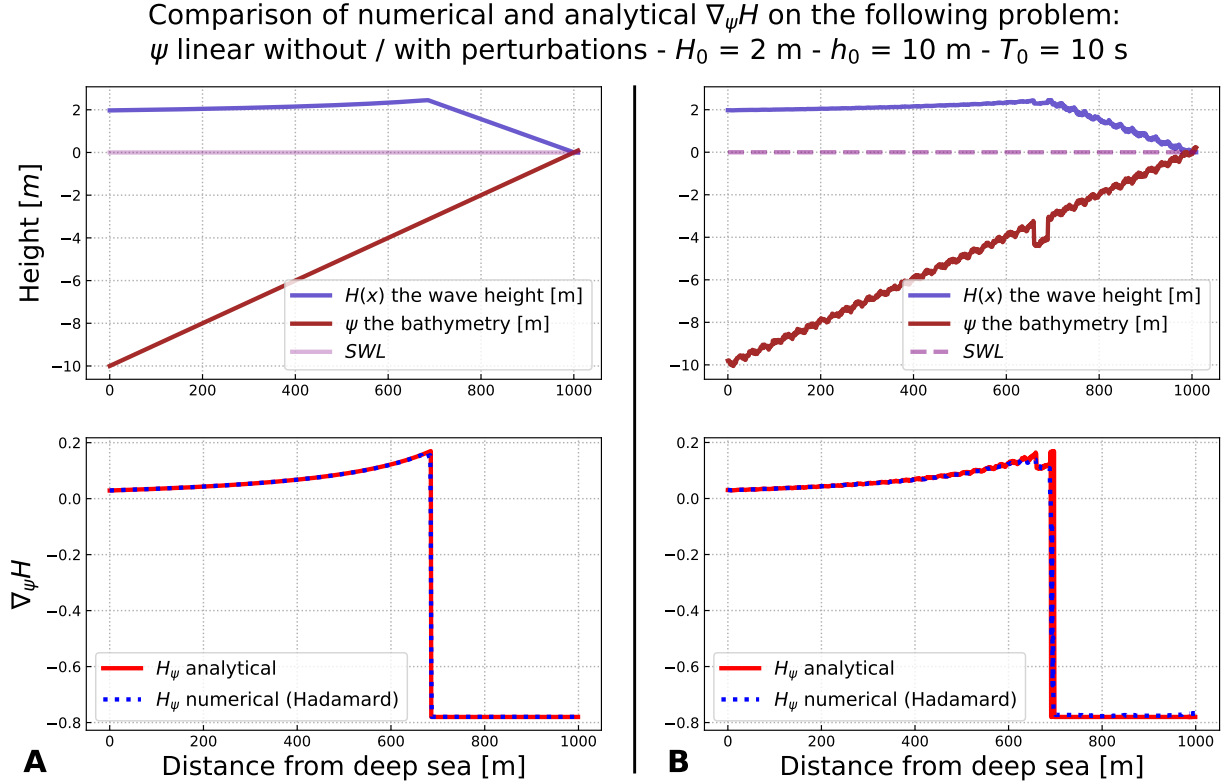


**Figure 3.4** – Comparison of numerical and analytical solution of  $\nabla_\psi H$  using OptiMorph model. Configuration without (A) / with (B) perturbations,  $H_0 = 2$  m,  $h_0 = 10$  m and the wave period  $T_0 = 10$  s. In dodgerblue, the wave height  $H$ , in brown the bottom profile  $\psi$ , in red  $\nabla_\psi H$  calculated analytically, in blue  $\nabla_\psi H$  calculated by Hadamard strategy.

We notice that the approximation is very good. There is still one point that has a defect in the non-linearity at  $x = 670$  m. However, this does not alter the morphodynamic results. To be sure of the robustness, we add non-linearity with a random function that induces perturbations. These are composed of sinusoidal functions and random translations between  $[-0.2, 0.2]$ , on the entire domain. We also set a hole at  $x = 650$  m. We obtain the simulation figure 3.4.B. Even with all these perturbations, the Hadamard approximation remains very robust.

## 4 Application of Hadamard Strategy

To go further, we can use the Hadamard strategy to couple any wave model to the morphodynamic model based on the gradient descent equation presented in (5.16). The figure 3.5 shows the detailed implementation of this coupling.

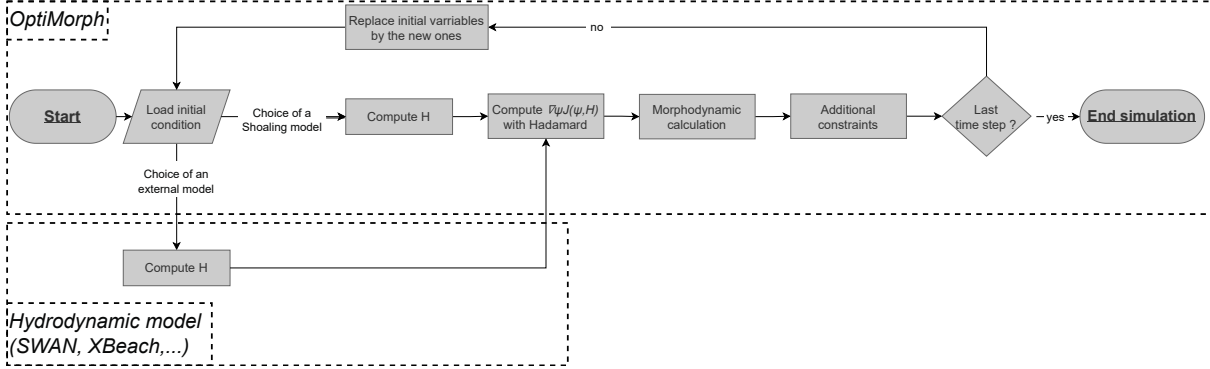


Figure 3.5 – OptiMorph workflow coupled with wave model.

Note that in all cases, it is necessary to calculate an averaged  $H$  to use it in the morphodynamic calculation. For spectral models such as SWAN and XBeach, this  $H$  is output directly from the model. However, wave-resolved models such as Shallow-Water 4.3 output a  $\eta$ . To integrate this quantity into the model, it must be averaged as a  $\eta_{RMS}$  with

$$\eta_{RMS} = \sqrt{\frac{1}{k T_0} \int_0^{k T_0} \eta^2 dt}, \quad k \in \mathbb{N} \quad (3.7)$$

and  $T_0$  the wave period. In this case, we have  $\eta_{RMS} \sim H$  provided that  $k$  is sufficiently large.

In this section, we perform Hadamard morphodynamics simulations forced by three distinct hydrostatic models: our extended shoaling model presented in appendix 3.4, SWAN and XBeach. Simulations are performed on 5 different experimental data sets: (i) one configuration from the SANDS experience (Eichentopf et al. 2018); (ii) one configuration from the LIP 11D experience flume experiment presented in table S.6 (part of the XBeach benchmark (Roelvink et al. 1995)); (iii) three from open-sea configurations with linear, concave and convex bottom profiles.

## 4.1 Description of Flumes Experiments

In this section, we briefly present the LIP 11D (Roelvink et al. 1995) and SANDS (Eichentopf et al. 2018) experiments. These morphodynamic experiments are necessary to validate our model.

### 4.1.1 The SANDS Experiments

The experimental setup for this study was conducted at the Canal d’Investigació i Experimentació Marítima (CIEM), a large-scale wave flume located within the Universitat Politècnica de Catalunya (UPC) in Barcelona, Spain. The CIEM is a large-scale wave

flume of 100 m length, 3 m width and 4.5 m depth with a working water depth of 2.47 m and 2.5 m. Waves were generated using a hydraulic wave paddle positioned at the end of the deep-water section in the wave flume. The initial beach profile was carefully crafted by hand using well-sorted, commercial sand with a narrow grain size distribution ( $d_{50} = 0.25$  mm,  $d_{10} = 0.154$  mm,  $d_{90} = 0.372$  mm), resulting in a measured sediment fall velocity of  $w_s = 0.034$  m/s. The active portion of the beach profile featured a slope of 1/15. The experimental configuration of the SANDS project in Barcelona was meticulously documented in (Alsina et al. 2011).

This experiment (Eichentopf et al. 2018) is composed of two parts, an erosive part on a linear beach with slopes 1/15 with a forcing of  $H_s = 0.53$  m and  $T_0 = 4.14$  s for an experiment duration of 23 hours and 30 minutes. An accretionary section on the final beach profile of the erosive section, with a forcing of  $H_s = 0.32$  m and  $T_0 = 5.44$  s for an experiment duration of 20 hours and 25 minutes.

#### 4.1.2 The LIP Experiments

The Large Installations Plan (LIP) experiments were conducted in the Delta Flume of Delft Hydraulics (now Deltares) (Roelvink et al. 1995), which is a large-scale facility measuring 225 x 7 x 5 m. During these experiments, various parameters such as water levels, wave-averaged velocity and suspended concentration profiles, orbital velocities, and bed levels were measured.

Three types of experiments were carried out in LIP under different types of irregular waves, resulting in three distinct beach states: stable (LIP 1A), erosive (LIP 1B), and accretive (LIP 1C).

In LIP 1A, the initial profile was linear with a slope of 1/30 and a median grain size of 0.22 mm. This part of the experiment represented a pre-storm event with the creation of a sedimentary bar under moderate wave conditions ( $H_s = 0.9$  m,  $T_0 = 5$  s).

The LIP 1B part of the experiment used the final profile from LIP 1A and represented a storm event with larger waves ( $H_s = 1.4$  m,  $T_0 = 5$  s). The bar moves seaward under the action of large waves, highlighting the physical process of erosion.

Finally, the LIP 1C part of the experiment used the final profile from LIP 1B and represented a post-storm event with smaller waves ( $H_s = 0.6$  m,  $T_0 = 8$  s). The bar moved back towards the coast asymmetrically, highlighting the physical process of accretion.

The bed profile was measured using a profile follower that used an automated sounding system. The LIP experiments provided valuable insights into the morphodynamic behaviour of sandy beaches under different wave conditions and have been widely used to validate numerical models of beach morphodynamics.

## 4.2 Hydro-Morphodynamic Results on Flume Experiment

To begin, we perform hydro-morphodynamic simulations with our morphodynamic approach using Hadamard's calculation of  $\nabla_{\psi}H$ . To highlight the phenomenological aspect of our model, we start by performing simulations on SANDS erosive experience (Eichentopf et al. 2018).

In this case, we set up the models as follows. We set a domain  $\Omega$  of 53 m in length with a uniform subdivision of 530 cells. For XBeach and SWAN, the incoming wave boundary condition is provided using a JONSWAP wave spectrum (Hasselmann et al. 1973), with a significant wave height of  $H_s = 0.53$  m and a peak frequency at  $f_p = 4.14$  s<sup>-1</sup>. For the extended shoaling model (appendix 3.4), we use directly  $H_s$  and a wave period  $T_0 = 4.14$  s. The breaker model of XBeach uses the D. J. Roelvink (1993) formulation, with a breaker coefficient of  $\gamma = 0.4$ , a power  $n = 15$ , and a wave dissipation coefficient of 0.5. The breaker model of SWAN is based on the Battjes et al. (1978) breaking parametrization and the extended Shoaling model is simply based on a Munk breaking criterion  $\gamma = 0.4$ . The mobility parameter  $Y$  of our morphodynamic model has a value of  $5 \times 10^{-3}$  m.s.kg<sup>-1</sup>. The model is set to run 23.5 h using a coupling time of 42.3 s. We compare the numerical results to those experimental data. The hydro-morphodynamic results are presented in figure 3.6.A and the differences between the final bottom profile  $\psi_f$  and initial bottom profile  $\psi_0$  are presented in figure 3.6.B. The reference is the experimental curve in dark red.

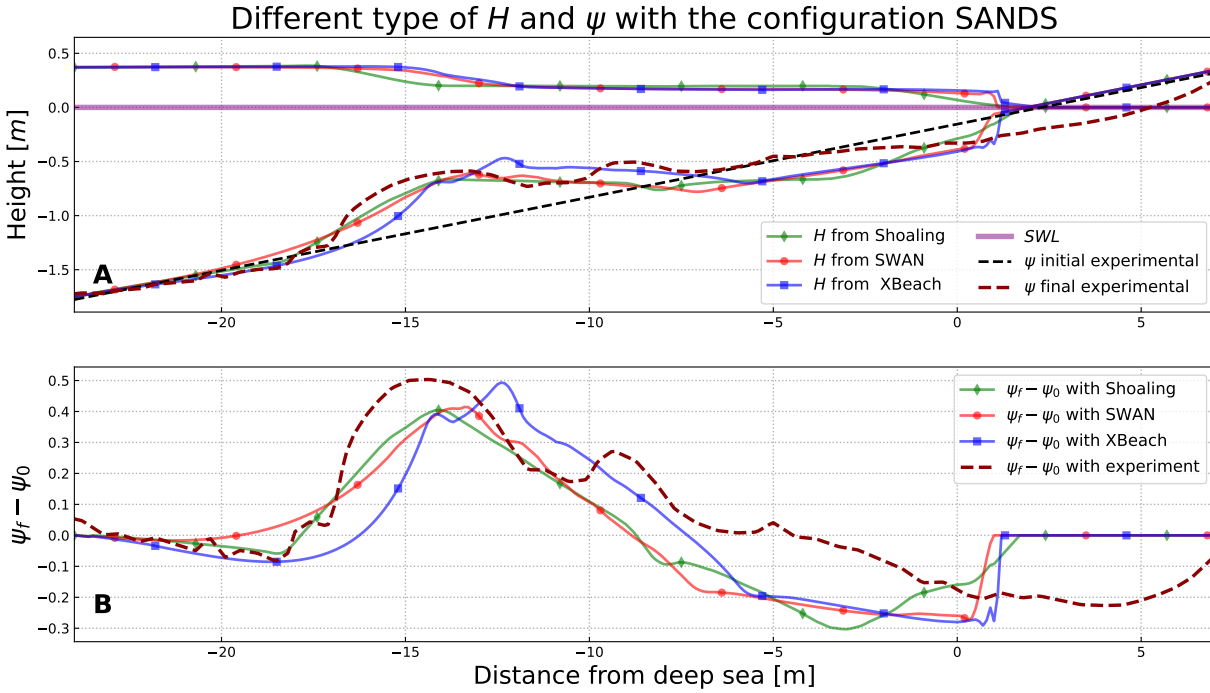


**Figure 3.6** – A) Hydro-Morphodynamic results obtained with OptiMorph model using Hadamard strategy with wave models (Shoaling (green), SWAN (red) and XBeach (blue)). Bottom profile configuration from the SANDS erosive experience. Black: bottom profile, green:  $H$  and  $\psi$  from improved shoaling with Hadamard strategy, red:  $H$  and  $\psi$  from SWAN with Hadamard strategy, blue:  $H$  and  $\psi$  from XBeach with Hadamard strategy, dark red:  $\psi$  from experience. B) Morphodynamic ecarts of  $\psi_f - \psi_i$  obtained with the Shoaling, SWAN, XBeach models and experiment. Bottom profile configuration from the SANDS channel experiment. In green: morphodynamic differences from shoaling with Hadamard strategy ( $\psi_{RMSE} = 11.7$  cm), red: morphodynamic differences from SWAN with Hadamard strategy ( $\psi_{RMSE} = 12.7$  cm), blue: morphodynamic differences from XBeach with Hadamard strategy ( $\psi_{RMSE} = 13.5$  cm), dark red: morphodynamic differences from the experiment.

In all three simulations and the experiment, a sedimentary bar is created over time and a trough is formed between the sandbar and the shore. These sedimentary bars are positioned below the breaking point of the wave. The sedimentary bars from the simulations have one main hump, whereas in the experiment there are two. In the simulations, the trough rises once the water has touched the shore ( $x = 1$  m), while in the experiment, the trough continues afterwards (up to  $x = 7$  m). The three simulations produce relatively similar results.

The next simulation from LIP - 1C flume experiment (Roelvink et al. 1995). In this other case, we set a domain  $\Omega$  of 180 m in length with a uniform subdivision of 180 cells. For XBeach and SWAN, the incoming wave boundary condition is provided using a JONSWAP wave spectrum (Hasselmann et al. 1973), with a significant wave height of  $H_s = 0.6$  m and a peak frequency at  $f_p = 8$  s<sup>-1</sup>. For the extended shoaling model (appendix 3.4), we use directly  $H_s$  and a wave period  $T_0 = 8$  s. The breaker model of XBeach, SWAN and extended Shoaling model are the same as in the previous simulation (still with  $\gamma = 0.4$ ). The mobility parameter  $Y$  of our morphodynamic model has a value of  $5 \times 10^{-3}$  m.s.kg<sup>-1</sup>. The model is set to run 13 h using a coupling time of 46.8 s.

We compare the numerical results to those experimental data. The hydro-morphodynamic results are presented in figure 3.7.A and the differences between the final bottom profile  $\psi_f$  and initial bottom profile  $\psi_0$  are presented in figure 3.7.B. The reference is the experimental curve in dark red.

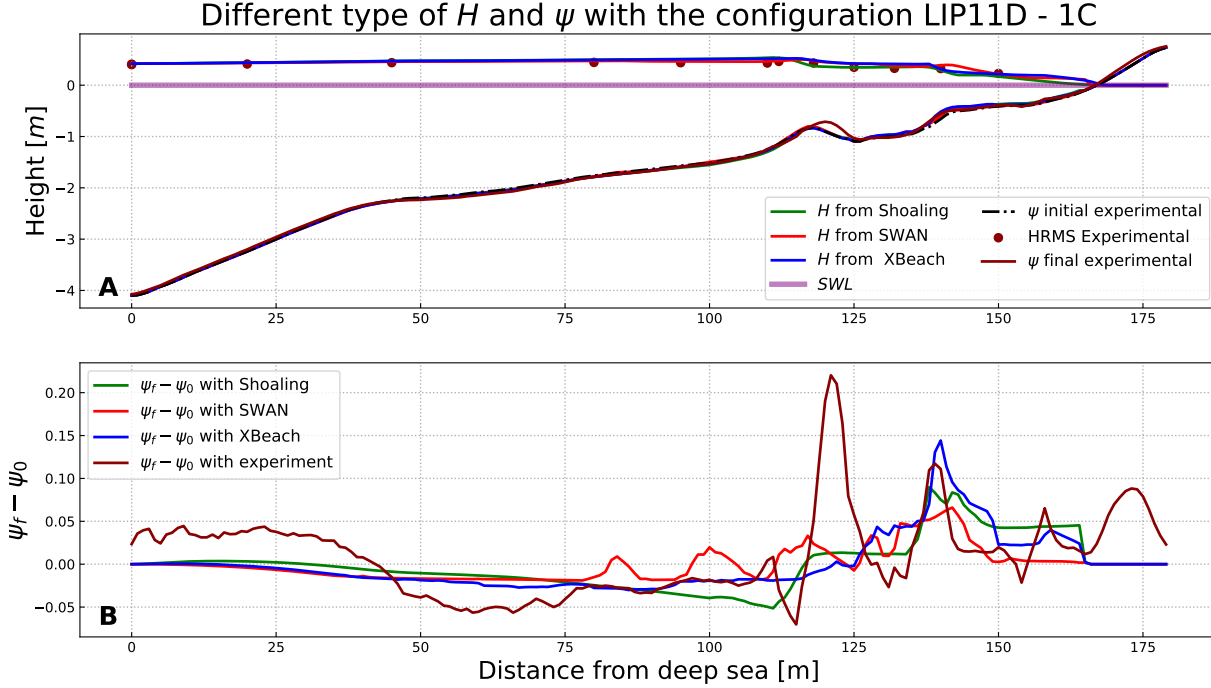


**Figure 3.7** – A) Hydro-Morphodynamic results obtained with OptiMorph model using Hadamard strategy with wave models (Shoaling (green), SWAN (red) and XBeach (blue)). Bottom profile configuration from the LIP 1C channel experiment. Red points: measured HRMS, black: bottom profile, green:  $H$  and  $\psi$  from improved shoaling with Hadamard strategy, red:  $H$  and  $\psi$  from SWAN with Hadamard strategy, blue:  $H$  and  $\psi$  from XBeach with Hadamard strategy, dark red:  $\psi$  from experience. B) Morphodynamic ecart of  $\psi_f - \psi_i$  obtained with the Shoaling, SWAN, XBeach models and experiment. Bottom profile configuration from the LIP 1C channel experiment. In green: morphodynamic differences from shoaling with Hadamard strategy, red: morphodynamic differences from SWAN with Hadamard strategy, blue: morphodynamic differences from XBeach with Hadamard strategy, dark red: morphodynamic differences from the experiment.

In this experiment, the outer sedimentary bar is moving towards the coast. None of the simulations reproduces this behaviour: the outer bars remain in the same place ( $x = 120$  m). In the experiment, the inner sediment bar grows ( $x = 140$  m). Simulations show very similar behaviour. The three simulations produce relatively similar results.

### 4.3 Hydro-Morphodynamic Results on Open-sea Configurations

In this section, we perform simulations in open-sea configurations. The bottom profiles are linear, concave and convex shapes. These shapes are not directly observable in nature but representative of several typical settings (dissipative, reflexive). Forth, they allow to observe if the morphodynamic model is able to reproduce the phenomenology of sedimentary evolution of sand beaches. For these cases, we perform our morphodynamic model using waves from SWAN, XBeach, extended Shoaling and Shallow-Water models.

In this configuration, we use the same model settings as before with the exception of a  $\Omega$  domain length resized at 600 m with a uniform subdivision in 600 cells. The forcing is no longer uniform but represents a storm event of 3 days with a peak wave height  $H_s=2$  m. The waves have a period of  $T_0 = 12$  s and the water depth at  $x = 0$  is  $h_0 = 20$  m. The



coupling time is set to 345 s. For the Shallow-Water model, the resolution is described in (Marche et al. 2007).  $\eta_{RMS}$  starts to be calculated after 10 simulated wave periods (10  $T_0$ , here 120 s). Then,  $\eta_{RMS}$  (defined in equation (3.7)) is averaged over 8 wave periods ( $k = 8$ ). The results of these simulations are presented in figure 3.8.

Evolution of  $\psi$  with different hydrodynamic models and different bottom profile  
 $H_0 = 2 \text{ m}$ ,  $T_0 = 12 \text{ s}$ ,  $h_0 = 20 \text{ m}$ ,  $\Omega = 600 \text{ m}$ , Dynamic forcing

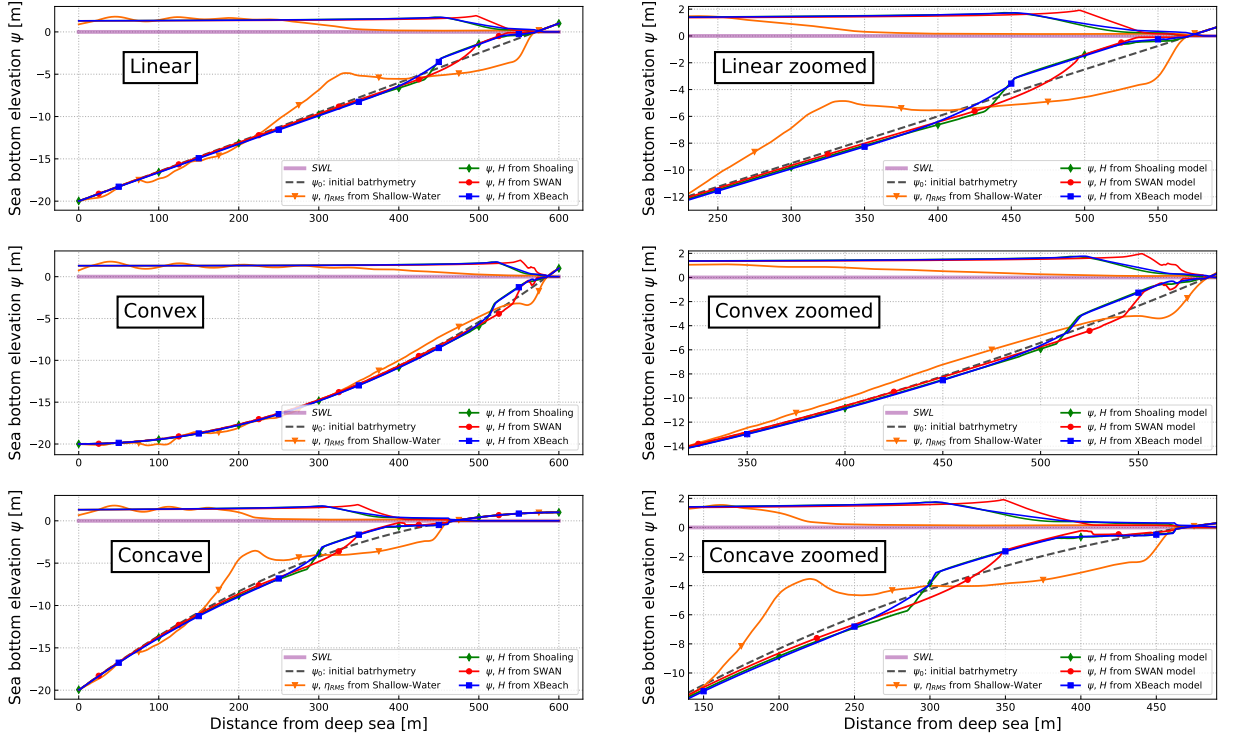


**Figure 3.8** – Evolution of  $\psi$  using Hadamard strategy with extended Shoaling (green), SWAN (red), XBeach (blue) and Shallow-Water (orange) models. Simulation on open-sea configuration with linear, convex and concave configurations. Simulation parameters of  $H_0 = 2 \text{ m}$ ,  $T_0 = 12 \text{ s}$ ,  $h_0 = 20 \text{ m}$ ,  $\Omega = 600 \text{ m}$ .

In all three cases of direct  $H_s$  calculation, the simulations produce very similar results. Depending on the angle of the slope, a sedimentary bar is observed more or less far from the shore. For a steep angle (convex beach), the sediment bar is very close to the shore; whereas for a slight angle (concave beach), the bar is further from the shore. All these sedimentary bars are all followed by a trough and are positioned below the breaking point of the wave. In the case of a convex profile, the sediment bar and the wave breaking, produced using SWAN, are closer to shore than the other two simulations.

In the case of the Shallow-Water model, the results are quite different: the sedimentary bar is larger, further from the shore and has a larger trough.

## 5 Discussion

### 5.1 Computation time

This section is devoted to the analysis of simulation times of the wave models and our morphodynamic calculation. Table 3.1 corresponds to the computation times for the LIP 11D - 1C simulations (section 4.2) with Hadamard strategy using the SWAN, XBeach and extended Shoaling models. XBeach was used for providing wave calculation only but this model also calculates the circulation. Therefore, it was necessary to run it over a longer time than that required by morphodynamics to get the right significant wave height  $H_s$ .

Simulation with 180 points	Hydrodynamic			Morphodynamic by gradient descent
	Shoaling	SWAN	XBeach	
Computation time for 1 iteration (s)	0.004	0.278	7.372	0.012
Total computation time for 1000 iterations (mins)	0.26	4.83	123.06	0.2

**Table 3.1** – Computation time with 180 points calculated: LIP11D - 1C with different wave models. Simulations made with a 2.4 GHz computer using a single core on an Intel Xeon E5-2680 processor.

We notice that the calculation time of the Shoaling model is very small (direct calculation in python); it is 50 times smaller than that of SWAN and XBeach. XBeach calculation times come from the circulation model, which has the advantage of giving the current  $u$  (contrary to SWAN) and could be used for another definition of  $\mathcal{J}$  functional. The morphodynamic calculation time is very small and negligible compared to the hydrodynamic (except shoaling). By increasing the mesh size to 1000 points (5 times more), we obtain the table 3.2.

Simulation with 600 points	Hydrodynamic			Morphodynamic by gradient descent
	Shoaling	SWAN	XBeach	
Computation time for 1 iteration (s)	0.013	0.7158	17.243	0.044
Total computation for with 1000 iterations (mins)	0.966	12.67	288.12	0.762

**Table 3.2** – Computation time with 600 points calculated with different wave models. Simulations made with a 2.4 GHz computer using a single core on an Intel Xeon E5-2680 processor.

The calculation times are also multiplied by 3. The computation time of the Shallow-Water model (presented in section 4.3) has not been shown as it is necessary to solve the model a very large number of iterations (corresponding to the simulation time of  $k T_0$  from equation (3.7)) in order to perform a single descent iteration.

To save computing time, we could use some interpolation strategy between the grid of the wave tool and that of the morphodynamic model. This would allow performing wave computations on grids with fewer points with the same final results.

## 5.2 Flume Simulation

This section is devoted to the morphodynamic behaviour of our model using the Hadamard strategy on flume configuration (Roelvink et al. 1995; Eichentopf et al. 2018). The main question is to check whether the numerical model is capable of reproducing the morphodynamic behaviours measured experimentally.

In the SANDS results shown in figure 3.6, we can see that a sediment bar is created from a linear beach profile (1/15). Although the simulations do not reproduce the sedimentary bar exactly like the experiment, they show very similar results. The sedimentary bar in the simulations is much shorter (in the sense of  $x$ ) than in the experiment. In the simulations, the pattern of troughs between the sediment bar and the shoreline is very similar to that in the experiment. However, in the experiment, the trough goes beyond the water level. This result cannot be observed in our model (except with a tide) as there is currently no mechanism to model this erosion beyond the water level. This induces errors in our model, which conserves the quantity of sand. This lack of sand could explain why our sedimentary bar is shorter than the experimental one.

In the LIP 1C results shown in figure 3.7, we notice that two main sandbars are observed. The inner one ( $x = 140$  m) seems to grow. The outer one ( $x = 120$  m) moves to the shore. The 3 simulations based on Hadamard strategy succeeded in reproducing the behaviour of the inner bar ( $x = 140$  m). XBeach model coupled to OptiMorph (blue) overestimates this sandbar and SWAN model coupled to OptiMorph (red) underestimates it. On this bar, there is a consequent loss of energy which induces a strong gradient and allows the bar to grow. However, none of the simulations has succeeded in reproducing the behaviour of the outer bar ( $x = 120$  m) moving towards the shore.

This is because, the parameterization of the sea bottom  $\psi$  and equation (5.16) describing its dynamics only accounts for vertical variations using the gradient of the functional with respect to the sea bottom shape. Therefore, no lateral translation can be predicted by this model. To be able to account for lateral displacements, we need to introduce transport mechanisms, though, for instance, the following modification of the model:

$$\begin{cases} \psi_t = Y \Lambda d - V \nabla_s \psi \\ \psi(t = 0) = \psi_0 \end{cases}, \quad (3.8)$$

where we have introduced a transport operator in the right-hand side.  $\nabla_s \psi$  is the spatial derivative of  $\psi$  along the mean slope of the sea bottom and  $V$  the velocity along this direction. We show the behaviour of the model using the following expression of  $V$  involving, the amplitude of orbital velocity at bottom  $U_b$  (Wiberg et al. 2008), and the

significant wave height  $H$ :

$$V = 0.01 U_b \left( \frac{H}{H_{max}} \right)^p \quad \text{with} \quad U_b = \frac{H \pi}{T_0 \sinh(kh)}. \quad (3.9)$$

The dimensionless morphodynamic factor 0.01 has been chosen in order to make the ranges of lateral and vertical variations comparable.

Figure 3.9.A illustrates the behaviour of this model for different  $p$  values. The best choice appears to be  $p = 1$  and as expected, the bar moves back towards the coast (asymmetrically) under smaller waves which shows that transport mechanisms were necessary. Velocity distribution figure 3.9.B shows that the transport mechanisms are mainly located around the two sandbars.

To go farther, and to make the approach generic, we should express this velocity  $V$  using the gradient of the functional as done for the vertical motion using the gradient of the functional with respect to the shape.

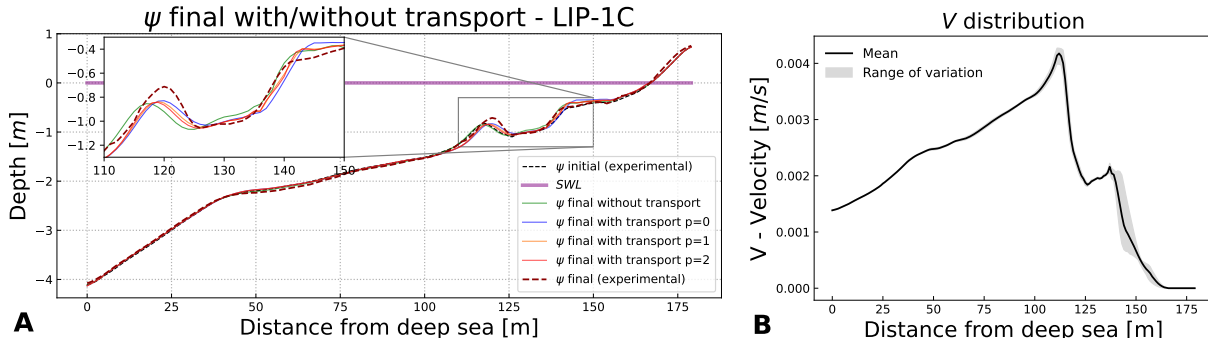


**Figure 3.9** – A) Morphodynamic results by the OptiMorph model augmented by the transport mechanisms for  $p = 0, 1, 2$  and the XBeach wave model, for the LIP 1C channel experiment. B) Velocity distribution for  $p = 1$ .

By comparing with hydro-morphodynamic models in the literature such as XBeach (D. J. Roelvink et al. 2009), we notice in figure 3.10 that for similar simulations (from the same benchmark),

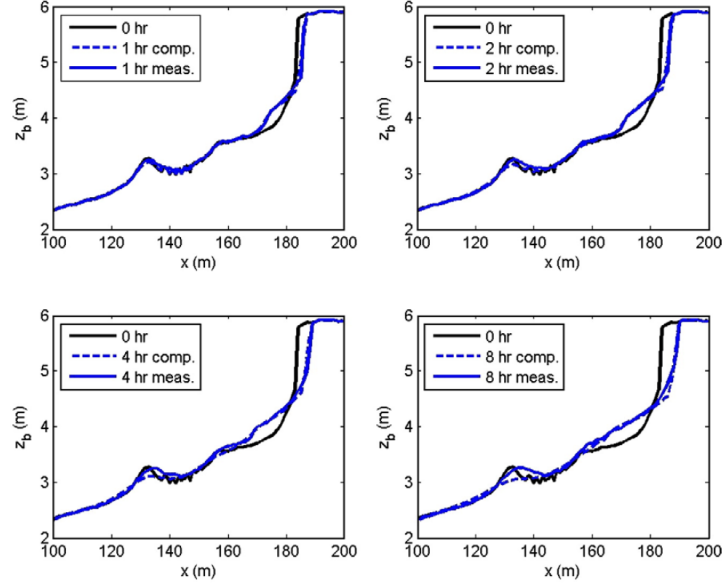


**Figure 3.10** – Figure from (D. J. Roelvink et al. 2009): Measured and modeled bed level (with XBeach) after 1, 2, 4 and 8 h of wave action, for a water level of 4.56 m above the flume bottom

XBeach did not reproduce the morphodynamic behavior of the first sandbar. Indeed, this one collapses whereas it should move towards the shore. However, the shoreline displacement are very good reproduced by XBeach. In fact, it is specified that XBeach is not a model that is supposed to reproduce the behavior of the bars but rather that of the troughs at the shoreline.

### 5.3 Open-Sea Simulation

This section is devoted to the morphodynamic behaviour of our model using the Hadamard strategy on open-sea configuration. The two simulations figures 3.6 and 3.8, show that there is a creation of the sandbar at the wave breaking point. Figure 3.8 shows that a slight pit is created before the sandbar and a trough one after. These observations are providing because they represent the major morphologic features along a typical sand bar profiles. Indeed, it is common to observe sedimentary bars at the wave breaking point. Moreover, the steeper the slope (convex), the later the breaking, the closer the sandbar is to the shore ( $x = 550$  m). Conversely, the gentler the slope (concave), the farther the breaking point, the farther the sandbar is from shore ( $x = 350$  m). These types of beach profiles are usually observed in nature (Wright et al. 1984). It highlights the fact that even with an unrealistic initial beach profiles, the model can produce a realistic beach profile without any need in pre-nucleation of the bottom perturbation. Forth, whatever the physics behind the wave spectral model, the morphodynamic model is able to produce very similar morphodynamic results. On the other hand, the results produced by

the Shallow-Water model are quite different, but no less realistic.

## 5.4 Gamma Sensibility

To highlight the creation of sandbars at the wave breaking point, we artificially change the breaking point by varying the W. Munk (1949) criterion  $\gamma$  on hydro-morphodynamic simulations using Hadamard strategy. These simulations are performed with the SWAN wave model (Booij et al. 1996; Reniers et al. 2022) and the same wave parameters as the simulation 4.3 ( $T_0 = 12$  s and  $H_0 = 2$  m). By taking the W. Munk (1949) criteria at the values 0.3, 0.4, 0.5, 0.6, 0.7, 0.8, we obtain the figure 3.11.

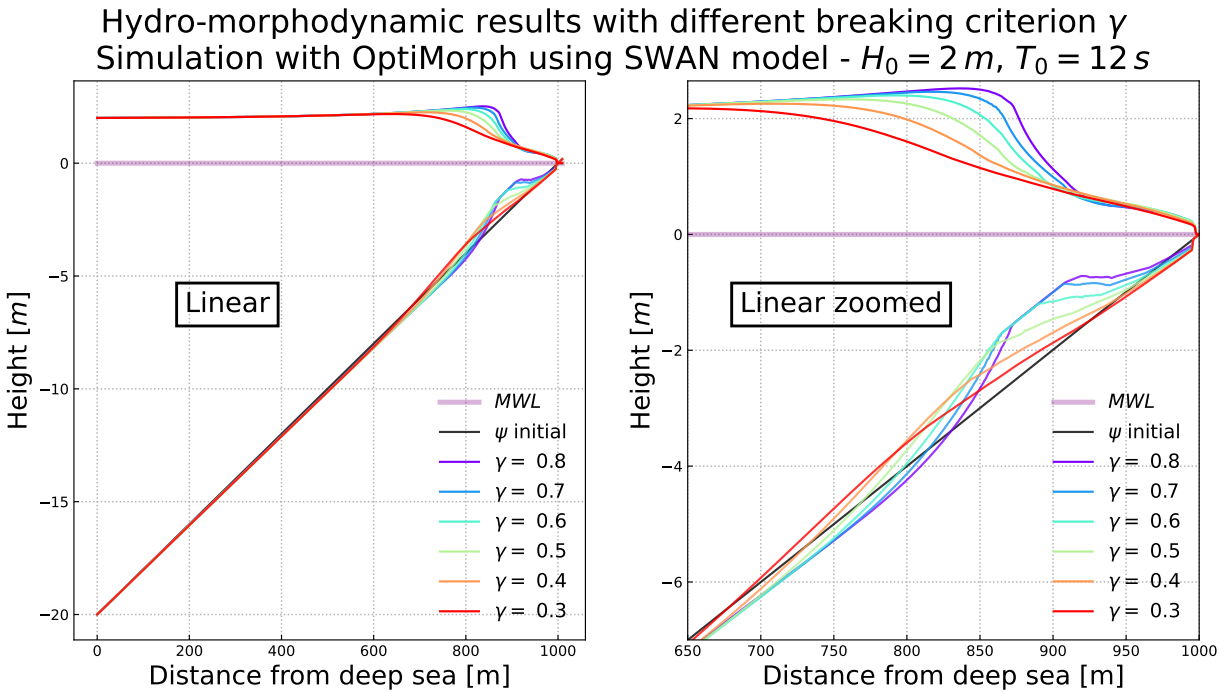


**Figure 3.11** – Hydro-morphodynamic results with different breaking criterion  $\gamma$  - Simulation with OptiMorph (Hadamard strategy) using SWAN model -  $H_0 = 2$  m,  $T_0 = 12$  s,  $h_0 = 20$  m.

The figure 3.11 shows that the sandbars are formed systematically at the wave breaking point. The higher the coefficient  $\gamma$ , the closer to the coast the waves break and the closer the sandbar is to the coast. Moreover, troughs at the lee side of the sandbar like observed in the nature are systematically nucleated (Wright et al. 1984).

## 5.5 Limitation of a Wave Resolving Model

Coupling our morphodynamic model with a wave resolving model has many limitations. The first is that computation times are much longer, as shown in the section 5.1. Secondly, it's much harder to get a breaking with this family of models. Under certain

conditions, these models have so much numerical dissipation that they do not mark the breaking. This is the case with our Shallow-Water model, taking a domain of  $\Omega = 600$  m and a medium beach slope as shown in figure 3.12.B. Furthermore, we note that  $\eta_{RMS}$  is very far from the other wave models.

### Comparison between $H$ and $\eta_{RMS}$ on the same scale

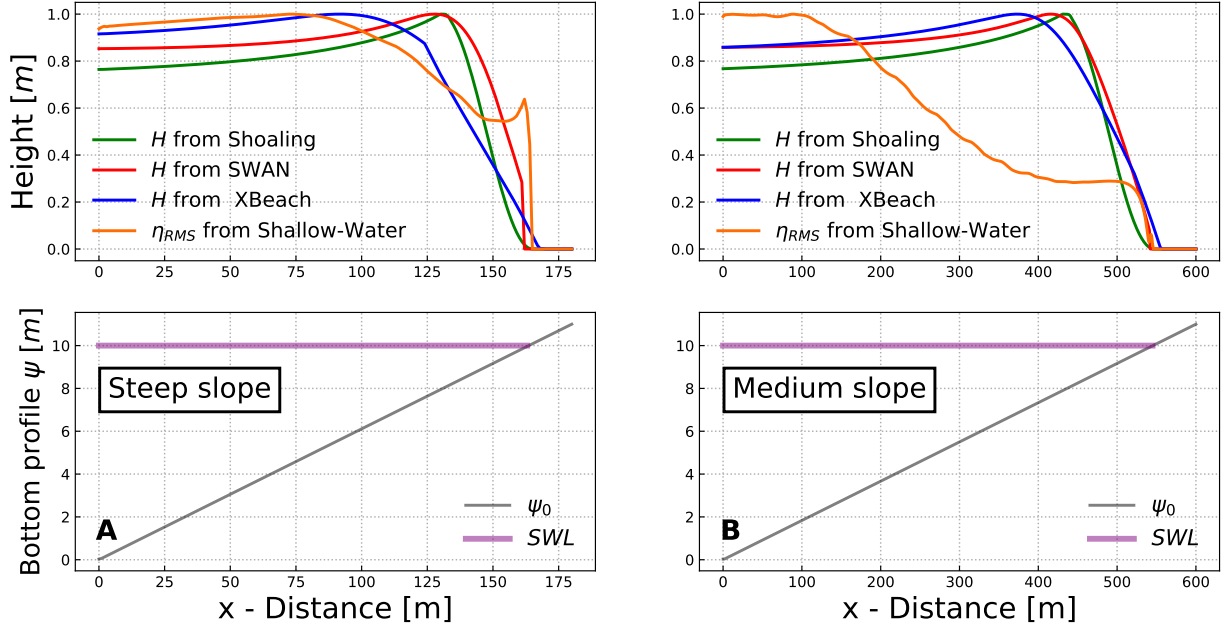


**Figure 3.12** – Comparison between  $H$  from models Shoaling (green), SWAN (red) XBeach (blue) and  $\eta_{RMS}$  from Shallow-Water (orange) models.  $H$  and  $\eta_{RMS}$  are on the same scale. A) Simulation parameters of  $H_0 = 1.5$  m,  $T_0 = 8$  s,  $h_0 = 20$  m,  $\Omega = 180$  m. B) Simulation parameters of  $H_0 = 1.5$  m,  $T_0 = 8$  s,  $h_0 = 20$  m,  $\Omega = 600$  m.

The previous section 5.4 shows that it is necessary to have a well-marked breaking in order to have a realistic morphodynamic response. In the case of a steep slope (figure 3.12.A), it is possible to have a marked breaking and therefore a coherent morphodynamic response.  $\eta_{RMS}$  is also quite close to the other wave heights. Once again, we notice that our model is conditioned by wave breaking.

## 6 Conclusion

In this chapter, we have described the Hadamard strategy that we have applied to our model. Using this approach, we calculate an approximation of the gradient  $\nabla_{\psi} \mathcal{J}$  of the functional  $\mathcal{J}$  with respect to the shape  $\psi$  without any additional wave calculation. This study allows us to differentiate any functional  $\mathcal{J}$  according to any input variable and relating to any wave model. The analytical and numerical comparisons performed prove that Hadamard strategy is accurate and robust. We applied this tool to realistic

and idealized hydro-morphodynamic simulations. This strategy is very powerful, as it can be applied to any shape optimization problem. The morphodynamic results with SANDS (Eichentopf et al. 2018) are very encouraging because they succeed in reproducing the dynamics of the dominant sedimentary bar. However, the initial results on LIP 1C (Roelvink et al. 1995) failed to reproduce the displacement of the outer sedimentary bar, although the behaviour of the inner was well reproduced. The model still needs to be improved in order to fix the lateral displacement and erosion above the water level. Nevertheless, our model is of low-complexity and reproduces the phenomenology as shown by the open-sea and SANDS results where it creates a bar at the breaking point without the need of a priori nucleation or pre-location of the bar.

#### Chapter key points

- A morphodynamic model by minimization that can be coupled with any wave model.
- Encouraging results on known morphodynamic benchmarks and open-sea configurations.
- An encouraging lead for lateral displacement.
- Reproduces certain natural coastal mechanisms (sandbars, erosion, ), our model is able to create realistic beaches with a bar at the breakpoint, starting from scratch.
- Hadamard is a new approach which allows to obtain easily and robustly  $\nabla_{\psi}\mathcal{J}$ . It can be used for general shape optimization.